ORIGINAL ARTICLE

Dynamics Modeling and Parameter Identification for a Coupled-Drive Dual-Arm Nursing Robot

Hao Lu[1] , Zhiqiang Yang[2,3], Deliang Zhu[2,3], Fei Deng[4] and Shijie Guo[2,3,4*]

Abstract

A dual-arm nursing robot can gently lift patients and transfer them between a bed and a wheelchair. With its light-weight design, high load-bearing capacity, and smooth surface, the coupled-drive joint is particularly well suited for these robots. However, the coupled nature of the joint disrupts the direct linear relationship between the input and output torques, posing challenges for dynamic modeling and practical applications. This study investigated the transmission mechanism of this joint and employed the Lagrangian method to construct a dynamic model of its internal dynamics. Building on this foundation, the Newton-Euler method was used to develop a dynamic model for the entire robotic arm. A continuously differentiable friction model was incorporated to reduce the vibrations caused by speed transitions to zero. An experimental method was designed to compensate for gravity, inertia, and modeling errors to identify the parameters of the friction model. This method establishes a mapping relationship between the friction force and motor current. In addition, a Fourier series-based excitation trajectory was developed to facilitate the identification of the dynamic model parameters of the robotic arm. Trajectory tracking experiments were conducted during the experimental validation phase, demonstrating the high accuracy of the dynamic model and the parameter identification method for the robotic arm. This study presents a dynamic modeling and parameter identification method for coupled-drive joint robotic arms, thereby establishing a foundation for motion control in humanoid nursing robots.

Keywords Nursing-care robot, Coupled-drive joint, Dynamic modeling, Parameter identification

1 Introduction

According to China's Seventh National Population Census, by the end of 2020, individuals aged 60 years and older constituted 18.7% of the population, with those aged 65 years and older representing more than 13.5% [1].

Amid the ongoing demographic shift towards an older population, coupled with declining birth rates, addressing the needs of seniors with disabilities has become a focal point in both societal discussions and scientific research [2]. Daily caregiving for these seniors covers a spectrum of activities ranging from changing clothes and feeding to bathing, managing excretion, assisting mobility, and lifting. It is particularly challenging to move seniors from beds to wheelchairs, bathrooms, or baths, which pose the greatest physical demand for caregivers [3, 4].

To address the challenges of patient transfer, leading research institutions have developed an array of nursing robots, including those designed for lifting [5], sliding [6], integrated bed-chair transitions [7], and humanoid back-hugging [8]. However, although specialized, these

*Correspondence:
Shijie Guo
guoshijie@fudan.edu.cn
[1] College of Electronic Information and Automation, Tianjin University of Science and Technology, Tianjin 300222, China
[2] Academy for Engineering & Technology, Fudan University, Shanghai 200433, China
[3] Shanghai Engineering Research Center of AI & Robotics, Shanghai 200433, China
[4] School of Mechanical Engineering, Hebei University of Technology, Tianjin 300130, China

Lu *et al. Chinese Journal of Mechanical Engineering*   (2024) 37:74

Page 2 of 15

robots present operational complexities and may fall short in providing the desired comfort and safety, thus narrowing their range of applications. Recently, dual-arm collaborative robots have emerged at the forefront, capturing attention because of their versatility, efficiency, and anthropomorphic design [9].

Recognizing this, researchers have seamlessly integrated dual-arm functionalities into nursing robots [10] and crafted models tailored for the elderly to aid in the transition between beds and wheelchairs. Designed with a focus on user comfort and safety, these robots are capable of handling heavy loads and achieving seamless human-machine collaboration and are also skillfully equipped to navigate complex, unstructured environments such as homes and hospitals [11].

Although dual-arm nursing robots have achieved notable research breakthroughs, they have not yet matured into products primed for widespread adoption [12]. A primary hindrance is the ill-fitting of traditional robotic arm designs for caregiving applications. Most nursing and rehabilitation robot joints use a single motor combined with a decelerator, making it difficult to generate sufficient torque to safely lift and support the human body [13]. Furthermore, the perpendicular orientation of the joint axes caused pronounced protrusions in the mechanical arm. This leads to an undue localized pressure upon human contact, thereby diminishing user comfort [14]. Therefore, it is crucial to move beyond conventional design approaches and delve into pioneering joint and structural designs of nursing robots.

In recent years, the field of research has seen growing interest in coupled drive joints [15]. By combining the output torques of multiple motors, this design significantly enhances the load-bearing capability of the joint, thus heralding a novel stride in joint technology [16]. Two primary configurations exist for this joint mechanism: rope−pulley and gear transmissions, with the former being predominant. Using coupled drive joint technology, Olarui launched a bipedal robot called Sherpa to enhance leg movement efficiency [17]. Hagn employed this approach to craft a Miro surgical robot, increasing the operational flexibility during surgery [18].

The dynamic establishment is crucial for robots to execute force control [19]. In conventional robot dynamics modeling, factors such as joint internal inertia and flexibility are often overlooked, leading to a straightforward correlation between the output torque of the motor and the joint response [20]. Although this simplification is acceptable for traditional collaborative robots with simplistic designs and negligible transmission inertia, it is not applicable for coupled-drive joints. Given their intrinsic coupling effects, ignoring their transmission inertia would be incorrect, necessitating

a deeper exploration of their internal dynamic frameworks. Research on dynamic modeling techniques for the coupled drive joints of robots is still in its nascent stage [21].

Nevertheless, valuable insights can be gained from studies focusing on differential transmission structures in sectors such as automobiles, wind power, and aircraft engines. Xiang et al. focused on the differential speed control of wind turbine systems and devised a triaxial dynamic model for their transmission mechanism. Using the Lagrangian approach, he derived the corresponding dynamic equations [22]. Similarly, Che et al. constructed dynamic equations for a wind turbine differential transmission system based on a multi-body dynamic framework [23].

In the real-world operation of robotic arms, beyond the effects of motor-driven torque, multiple nonlinear disturbances are encountered, with frictional forces being particularly influential on the arm's motion dynamics [24, 25]. Friction arises from a combination of factors, such as relative velocity, acceleration, displacement, lubrication status, and contact conditions, and is present at every moving interface [26]. For simplicity, when devising a friction model, it is customary to localize the frictional force at the pivot point of the joint, representing it as a function primarily tied to the speed [27]. Traditional friction models, either discontinuous or segmented in continuity, present challenges in accurately describing friction as speed approaches zero [28]. This can result in undesirable vibrations and jolting during directional shifts.

This study introduces a novel coupled-drive nursing robot aimed at enhancing the safety and comfort of human-robot interactions. For this design, we conducted in-depth dynamic modeling of the coupled-drive joints and a robotic arm composed of these joints. To precisely address the joint friction and impacts during direction changes, we integrated a continuous and differentiable friction model into the dynamic equations. Based on this model, we linearize the dynamic equations and derive a minimal set of inertia parameters. Furthermore, we established a mapping between the frictional force and the motor current using a particle swarm optimization algorithm to identify the parameters of the continuous friction model. Additionally, we optimized the excitation trajectory and employed machine-learning techniques to identify the inertia parameters of the robotic arm. In the final phase of this study, we set up an experimental platform and conducted trajectory-tracking experiments, the results of which validated the high accuracy of our dynamic model and parameter identification.

2 Design and Kinematic Analysis of Coupled Drive Nursing Robots

2.1 Coupled Drive Nursing Robot Design

In this study, a novel coupled drive joint was designed to meet the requirements for large-area human-machine contact. The joint employs two motors as the inputs and achieves a coupled output through a differential transmission mechanism comprising three equal-diameter bevel gears, as shown in Figure 1.

This joint provides dual rotational flexibility for both pitch and rotation. Harnessing the combined output torque of the two motors significantly boosted their load-bearing capacity. Its sleek, cylindrical design ensures a smooth exterior devoid of protrusions 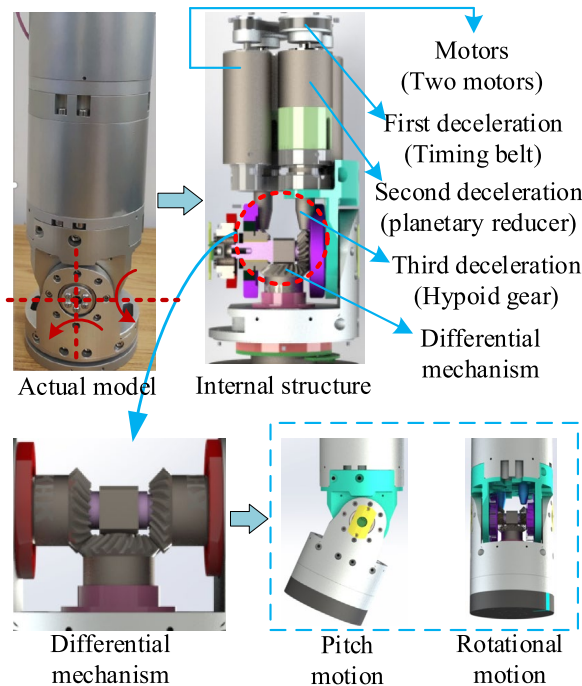for comfortable human interaction and maintains a compact form, mirroring the diameter of a human arm. Linking three of these joints yielded a robotic arm with six degrees of freedom. Additionally, with the integration of the designed waist, hip joints, and mobile platform, we established a comprehensive dual-arm transfer nursing robot. The complete design of the dual-arm nursing robot is shown in Figure 2.

2.2 Coupled Transmission Principle Analysis

In the study of coupled transmissions, we can skip the drive chain from the motor to the input bevel gear and delve directly into the differential mechanism. This setup comprises three uniformly sized bevel gears and a linkage rod. Bevel gears 1 and 2 serve as the input, while bevel gear 3, along with rod *H*, form the output. From a structural standpoint, this configuration aligns with the 2K-H type differential gear system, as shown in Figure 3.

As shown in Figure 3, ϕ_1 and ϕ_2 denote the angles of the two input bevel gears, whereas q_1 and q_2 correspond to the output angles for rotation and pitch. The direction in which the input bevel gears rotate determines the output's degrees of freedom (DOF). When both gears rotate at identical speeds in the same direction, only the pitch degree of freedom is activated. Conversely, if they spin at the same rate, but in opposite directions, only the rotational degree becomes active. In any other scenario, the joint produces outputs for both the pitch and rotation, leading to a coupled motion.

For the kinematic analysis, we selected two output angles from the coupled drive joint as the generalized coordinates, denoted q_1 and q_2. Consequently:

$$\dot{q}_1 = \omega_3, \dot{q}_2 = \omega_H, \tag{1}$$

where ω_3 and ω_H represent the angular velocities of bevel gear 3 and the linkage rod, respectively.

Figure 1 Coupled-Drive Joint

Motors (Two motors)
First deceleration (Timing belt)
Second deceleration (planetary reducer)
Third deceleration (Hypoid gear)
Differential mechanism

Actual model   Internal structure

Differential mechanism   Pitch motion   Rotational motion

Robot arms
Lumbar joint
Hip joint
Dexterous hand
Walking chassis

Coupled-Drive Joint   Nursing robot model   Nursing robot appearance   Nursing robot holding service   Degree of Freedom Configuration

Figure 2 Nursing robot using coupled-drive joints

Figure 3 Coupled drive principle

Figure 4 Coordinate system of the robotic arm
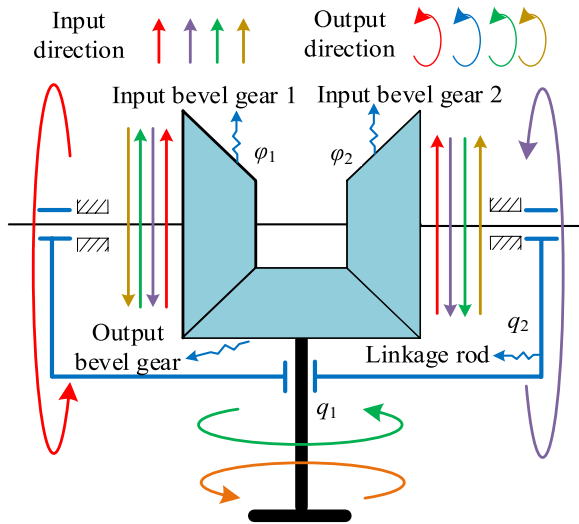
Using the calculated transmission ratio for the rotary gear system, we performed a kinematic analysis of the coupled drive joint as follows:

$$
\begin{cases}
i_{12}^H = \dfrac{\omega_1 - \omega_H}{\omega_2 - \omega_H} = -\dfrac{z_3 z_2}{z_1 z_3} = -\dfrac{z_2}{z_1}, \\
i_{13}^H = \dfrac{\omega_1 - \omega_H}{\omega_3} = \dfrac{z_3}{z_1},
\end{cases}
\tag{2}
$$

where i_{12}^H and i_{13}^H denote the transmission ratios between bevel gears 1 and 2 and bevel gears 1 and 3, respectively, when the reverse angular velocity $-\omega_H$ is applied to the linkage rod. z_1, z_2, and z_3 denote the tooth counts on the bevel gears; $z_1 = z_2 = z_3$. By merging Eqs. (1) and (2), we establish a link between the generalized coordinate velocity and the input speed of the bevel gear. Following the integration process, the kinematic decoupling relationship of the coupled drive joint was identified.

$$
\begin{cases}
q_1 = (\varphi_1 - \varphi_2)/2, \\
q_2 = (\varphi_1 + \varphi_2)/2, \\
\varphi_1 = q_1 + q_2, \\
\varphi_2 = -q_1 + q_2.
\end{cases}
\tag{3}
$$

2.3 Kinematic Analysis of the Robotic Arm

While the robot joints exhibited coupled movements, the robotic arm architecture comprised six sequentially connected rotational DOF. We employed a refined D-H parameter method to outline the kinematic model of the robot. The foundational coordinate system was anchored at the base joint of the robotic arm, with the z_0 axis extending vertically, the x_0 axis perpendicular to z_0 and oriented inward towards the plane of the paper, and the y_0 axis direction set by the right-hand rule. The
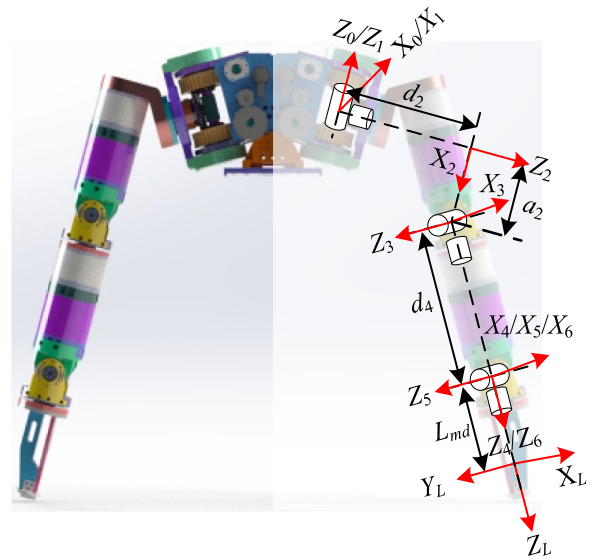
six subsequent coordinate systems, O_i-$X_iY_iZ_i$ ($i = 1$–6), were designated for each rotating joint, as shown in Figure 4. Note that the left and right arms of the nursing robot mirror each other in terms of structure and spatial orientation. For clarity, our analysis focused primarily on the kinematic attributes of the right arm.

Figure 4 shows the locations of the six rotational axes of the robotic arm. Each coordinate system was seamlessly integrated with its respective fundamental components. Within this context, θ_i signifies the joint variable, d_i indicates the link offset, a_{i-1} represents the link length, and α_i designates the link twist angle. Table 1 lists a detailed breakdown of the D−H parameters of the robotic arm.

The following parameters were set in the design of the nursing robot used in this study: $a_2 = 110$ mm, $d_2 = 242$ mm, and $d_4 = 28$ mm. Upon establishing the joint angles θ_i ($i = 1$–6), we can employ the kinematic equations to derive the pose matrix for the end effector of the robotic arm.

Table 1 D-H parameters of the robotic arm

Joint number	θ_i (rad)	d_i (mm)	a_{i-1} (mm)	α_{i-1} (°)	Angular range
1	θ_1	0	0	0	$[-0.5\pi, 0.5\pi]$
2	θ_2	d_2	0	90	$[-\pi, \pi]$
3	θ_3	0	a_2	-90	$[-0.5\pi, 0.5\pi]$
4	θ_4	d_4	0	-90	$[-\pi, \pi]$
5	θ_5	0	0	90	$[-0.5\pi, 0.5\pi]$
6	θ_6	0	0	-90	$[-\pi, \pi]$

3 Dynamic Modeling of the Nursing Robot
3.1 Dynamic Model of Coupled Drive Joint
After investigating the force transmission dynamics of the coupled drive joint, we embarked on dynamic modeling. Considering its distinct transmission features, we divided the joint transmission chain into two primary sections: fixed-axis transmission and differential transmission. The former spans from the motor to the pseudo-hyperbolic gear, whereas the latter bridges the input bevel gear to the output bevel gear and the linkage rod. Note that the output of the fixed-axis section is seamlessly integrated as an input to the differential section. Given the unwavering positions of the components within the fixed-axis section and input bevel gear, they can collectively be viewed as an integrated entity. Therefore, the joint aptly mirrors a differential mechanism bifurcated into two pathways: the left and right branches. A simplified transmission diagram of the coupled-drive joint is shown in Figure 5.

Using the Lagrangian approach [29], we executed dynamic modeling of the coupled drive joint. When integrated with the kinematic relationship of the joint (as described in Eq. (3)), the kinetic energy of the differential mechanism can be expressed as follows:

$$E = \frac{1}{2}J_{11}\dot{q}_1^2 + J_{12}\dot{q}_1\dot{q}_2 + \frac{1}{2}J_{22}\dot{q}_2^2,$$
$$\begin{cases} J_{11} = J_1 + J_2 + J_3, \\ J_{12} = J_1 - J_2, \\ J_{22} = J_1 + J_2 + J_H + m_3 r_H^2, \end{cases} \tag{4}$$

where J_1 and J_2 correspond to the equivalent moments of inertia from Motor 1 to Bevel Gear 1 and Motor 2 to Bevel Gear 2, respectively. J_3 and J_H denote the moments of inertia for Bevel Gear 3 and the linkage rod,
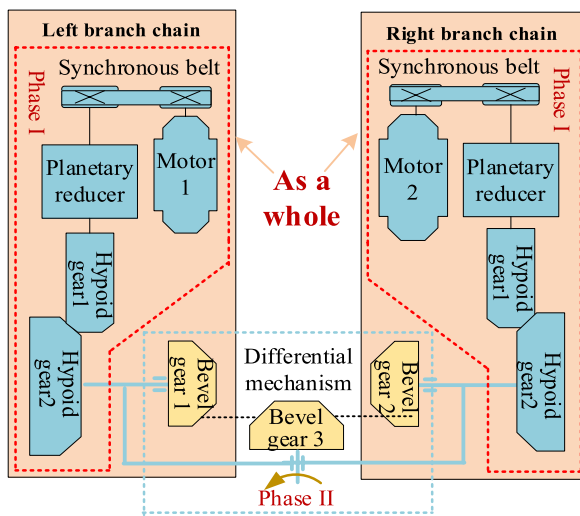

Figure 5 Simplified transmission diagram of the coupled drive joint

respectively. m_3 signifies the mass of Bevel Gear 3, and r_H represents the radius at which the center of mass of Bevel Gear 3 rotates around the axis of the linkage rod. The kinetic energy E of the system is differentiated with respect to the generalized coordinate velocities and generalized coordinates as follows:

$$\begin{cases} \frac{\partial E}{\partial \dot{q}_1} = J_{11}\dot{q}_1 + J_{12}\dot{q}_2, \\ \frac{\partial E}{\partial \dot{q}_2} = J_{12}\dot{q}_1 + J_{22}\dot{q}_2, \\ \frac{d}{d_t}(\frac{\partial E}{\partial \dot{q}_1}) = J_{11}\ddot{q}_1 + \frac{\partial J_{11}}{\partial q_1}\dot{q}_1^2 + \frac{\partial J_{11}}{\partial q_2}\dot{q}_1\dot{q}_2 \\ \qquad\qquad + J_{12}\ddot{q}_2 + \frac{\partial J_{12}}{\partial q_1}\dot{q}_1\dot{q}_2 + \frac{\partial J_{12}}{\partial q_2}\dot{q}_2^2, \\ \frac{d}{d_t}(\frac{\partial E}{\partial \dot{q}_2}) = J_{12}\ddot{q}_1 + \frac{\partial J_{12}}{\partial q_1}\dot{q}_1^2 + \frac{\partial J_{12}}{\partial q_2}\dot{q}_1\dot{q}_2 \\ \qquad\qquad + J_{22}\ddot{q}_2 + \frac{\partial J_{22}}{\partial q_1}\dot{q}_1\dot{q}_2 + \frac{\partial J_{22}}{\partial q_2}\dot{q}_2^2, \\ \frac{\partial E}{\partial q_1} = \frac{1}{2}\frac{\partial J_{11}}{\partial q_1}\dot{q}_1^2 + \frac{1}{2}\frac{\partial J_{22}}{\partial q_1}\dot{q}_2^2 + \frac{\partial J_{12}}{\partial q_1}\dot{q}_1\dot{q}_2, \\ \frac{\partial E}{\partial q_2} = \frac{1}{2}\frac{\partial J_{11}}{\partial q_2}\dot{q}_1^2 + \frac{1}{2}\frac{\partial J_{22}}{\partial q_2}\dot{q}_2^2 + \frac{\partial J_{12}}{\partial q_2}\dot{q}_1\dot{q}_2. \end{cases} \tag{5}$$

The potential energy U of the system can be expressed as follows:

$$U = -m_{He}gr_{He}\cos q_2 - m_3gr_H, \tag{6}$$

where m_{He} represents the mass of all components involved in the rotational motion, r_{He} denotes the distance from the centroid to the zero-potential energy surface, and g is the gravitational acceleration. The partial derivative of the potential energy U with respect to the generalized coordinates is expressed as follows:

$$\frac{\partial U}{\partial q_1} = 0, \quad \frac{\partial U}{\partial q_2} = m_{He}gr_{He}\sin q_2. \tag{7}$$

The power P of the system can be expressed as follows:

$$\begin{aligned} P &= Q_1\dot{q}_1 + Q_2\dot{q}_2 \\ &= T_1\omega_1 + T_2\omega_2 + T_3\omega_3 + T_H\omega_H, \end{aligned} \tag{8}$$

where Q_1 and Q_2 represent the generalized forces and T_1, T_2, T_3, and T_4 denote the input and output torques, respectively. By incorporating the kinematic relationships, the generalized force can be expressed as follows:

$$\begin{cases} Q_1 = T_1 - T_2 + T_3, \\ Q_2 = T_1 + T_2 + T_H, \end{cases} \tag{9}$$

Substituting Eqs. (5), (9), and (7) into the Lagrangian equation, the dynamics of the coupled drive joint can be expressed as follows:

$$J\ddot{q} + Gq = \tau, \tag{10}$$

where J represents the inertia matrix, G denotes the gravity matrix, and τ signifies the generalized force matrix.

$$\begin{cases} J = \begin{bmatrix} J_{11} & J_{12} \\ J_{12} & J_{22} \end{bmatrix}, \\ G = \begin{bmatrix} 0 & 0 \\ 0 & m_{He}gr_{He}\sin q_2 \end{bmatrix}, \\ \ddot{q} = \begin{bmatrix} \ddot{q}_1 \\ & \ddot{q}_2 \end{bmatrix}, \ \tau = \begin{bmatrix} Q_1 \\ Q_1 \end{bmatrix}. \end{cases} \quad (11)$$

Parameters, including the moment of inertia, mass, and location of the center of mass for each component within the joint, can be precisely determined using 3D design software, as listed in Table 2.

3.2 Dynamic Model of the Nursing Robotic Arm

Coupling was present within the joint; however, the robotic arm maintained a multi-link serial configuration. For the dynamic modeling of such arms, the predominant methods are the Newton-Euler and Lagrangian approaches. We opted for the Newton-Euler technique because it eliminates the need for partial derivatives of the joint angles in the calculations and offers a more straightforward programming implementation. To streamline the derivation, we set aside the influence of friction, which leads us to a relationship focused solely on the link factors between the joint output torque and joint angle.

$$M(q)\ddot{q} + C(q,\dot{q})\dot{q} + G(q) + \tau_{ext} = \tau, \quad (12)$$

where $M(q)$ represents the inertia matrix; $C(q,\dot{q})$ denotes the Coriolis and centrifugal force matrices; $G(q)$ denotes the gravitational matrix; τ_{ext} denotes the external force matrix; and τ represents the joint torque matrix.

3.3 Friction Model

The traditional friction model becomes non-differentiable at zero, creating uncertainties when describing the frictional forces at zero velocity. Such nuances result in oscillations and directional shifts in the controllers

Table 2 Joint component parameters

Parameter	Value	Parameter	Value
J_1	6.92×10^4 kg·mm^2	m_3	0.285 kg
J_2	6.92×10^4 kg·mm^2	r_H	52.3 mm
J_3	2.15×10^2 kg·mm^2	m_{He}	0.608 kg
J_H	5.17×10^2 kg·mm^2	r_{He}	45.97 mm

grounded in these models. To mitigate this challenge, this study integrated the continuous friction model introduced by Makkar [30]. This model is consistently differentiable across the time domain, and it is notably versatile and adeptly addresses the anisotropic challenges in frictional forces stemming from varying sliding directions. The continuous differentiable friction model is expressed as follows:

$$\begin{aligned} \tau_f(\dot{q}) = \gamma_1(\tanh(\gamma_2\dot{q}) - \tanh(\gamma_3\dot{q})) \\ + \gamma_4\tanh(\gamma_5\dot{q}) + \gamma_6\dot{q}, \end{aligned} \quad (13)$$

where γ_k ($k=1$–6) represents the coefficient of the continuous differentiable friction model. By incorporating this friction model into the dynamic model of the robotic arm, the dynamic equation can be expressed as follows:

$$M(q)\ddot{q} + C(q,\dot{q})\dot{q} + G(q) + \tau_f + \tau_{ext} = \tau, \quad (14)$$

where τ_f represents the friction torque.

3.4 Linearization of Dynamic Models

Linearizing the dynamic model of the robotic arm means expressing the torque within it as a product of the coefficient matrix and inertia parameters. Although conventional friction models are typically linearized alongside the dynamic model, the complexity of the continuous friction model led us to defer its linearization and identify the friction model parameters later. While ensuring the elements in τ remain unchanged, we have adjusted the parameter positions in the dynamic model as follows:

$$\tau = Y(q,\dot{q},\ddot{q})U, \quad (15)$$

where, U represents the inertia parameters of the robot, and Y represents the coefficient matrix. A single joint consists of 10 inertia parameters, resulting in 60 inertia parameters for a robotic arm with six degrees of freedom. However, owing to the structural constraints on the relative motion of the joints, the Y matrix is not always full rank [31]. This means that we cannot identify every element in U but can only recognize a set of minimal inertia parameters. Therefore, we derived a dynamic model based on this minimal set of inertia parameters, allowing the model to be further expressed as follows:

$$\tau = \tilde{Y}(q,\dot{q},\ddot{q})U_{\min}, \quad (16)$$

where $\tilde{Y}(q,\dot{q},\ddot{q})$ represents the column full-rank coefficient matrix obtained through $Y(q,\dot{q},\ddot{q})$ decomposition and $U_{\min}$ denotes the minimal set of inertia parameters. Using the method proposed by Gautier and Kawasaki [32], which derived the minimal inertia parameter set through categorical reorganization, we identified 36

Table 3 Minimum inertia parameter set

Joint	Parameter set						
1	0	0	0	0	I_{zz1}	0	0
2	I_{xx2r}	I_{xy2r}	I_{xz2}	I_{yz2}	I_{zz2r}	mx_{2r}	my_{2r}
3	I_{xx3r}	I_{xy3}	I_{xz3}	I_{yz3}	I_{zz3r}	mx_3	my_{3r}
4	I_{xx4r}	I_{xy4}	I_{xz4}	I_{yz4}	I_{zz4r}	mx_4	my_{4r}
5	I_{xx5r}	I_{xy5}	I_{xz5}	I_{yz5}	I_{zz5r}	mx_5	my_{5r}
6	I_{xx6r}	I_{xy6}	I_{xz6}	I_{yz6}	I_{zz6}	mx_6	my_6

parameters in the minimal set. The minimum inertia parameters are listed in Table 3.

4 Parameter Identification

4.1 Parameter Identification of Friction Model

Typically, friction is gauged by assessing the torque output of the joints of a robot during steady movement. Without a torque sensor, the output can be inferred from the current readings of the motor, providing an indirect measure of friction. Dynamic variations in a robot's joints can result in inconsistencies in motor current data. To derive a more accurate measure of friction, it is essential to filter out factors such as inertia, Coriolis force, centrifugal force, gravity, and external forces using kinematic principles.

When the pitch movement axis was aligned perpendicular to the ground, the gravitational impact on the coupled drive joint remained steady. This specific orientation could be used to counteract the influence of gravity. During consistent motion without external loads, the joint acceleration is nullified, ensuring that the product of inertia and acceleration remains zero. This suggests that steady motion can effectively neutralize the effects of inertia. When the joint engages in a steady back-and-forth movement restricted to the pitch motion, the correlation between friction and torque produced by the motor is expressed as follows:

$$\begin{cases} \tau_{f1}(\dot{q}) + \tau_{n1}(\dot{q}) = T_1(\dot{q}) - T_2(\dot{q}), \\ \tau_{f1}(-\dot{q}) + \tau_{n1}(-\dot{q}) = T_1(-\dot{q}) - T_2(-\dot{q}), \end{cases} \quad (17)$$

where τ_{n1} represents the modeling error of friction during pitch motion. When the joint engages in a steady back-and-forth movement restricted to rotational motion, the correlation between the friction and torque produced by the motor is expressed as follows:

$$\begin{cases} \tau_{f2}(\dot{q}) + \tau_{n2}(\dot{q}) = T_1(\dot{q}) + T_2(\dot{q}), \\ \tau_{f2}(-\dot{q}) + \tau_{n2}(-\dot{q}) = T_1(-\dot{q}) + T_2(-\dot{q}), \end{cases} \quad (18)$$

where τ_{n2} represents the modeling error of friction during rotational motion. Potential modeling errors may arise from assembly variances, observational biases, or temperature shifts. Although these inaccuracies were not

governed by the speed magnitude, they were influenced by its direction as follows:

$$\begin{cases} \tau_{fi}(-\dot{q}) = -\tau_{fi}(\dot{q}), \\ \tau_{ni}(-\dot{q}) = \tau_{ni}(\dot{q}). \end{cases} \quad (19)$$

Therefore, by executing oscillatory movements and integrating their outcomes, the modeling discrepancies can be minimized. Once the gravity, inertia, and modeling discrepancies are considered and removed, the correlation between the friction and torque output of the motor is expressed as follows:

$$\begin{cases} \tau_{f1}(\dot{q}) = (T_1(\dot{q}) - T_2(\dot{q}) - T_1(-\dot{q}) + T_2(-\dot{q}))/2, \\ \tau_{f2}(\dot{q}) = (T_1(\dot{q}) + T_2(\dot{q}) - T_1(-\dot{q}) - T_2(-\dot{q}))/2. \end{cases} \quad (20)$$

Given the complexities associated with fully mitigating the effects of friction during the movement of a robotic arm, we implemented a phased identification strategy. This method focused on individually assessing the frictional forces of each coupled drive joint. It is important to note that all the coupled drive joints followed identical experimental and identification protocols. For illustrative purposes, we elaborate on this using a coupled drive joint situated at the forearm as a representative example.

We configured the pitch output to move uniformly within the $[-0.5\pi, 0.5\pi]$ interval. The joint initiated its movement at a pace of 1°/s. With each reciprocating motion, the speed was increased by 0.5°/s, interspersed with a 5-second interval. This regimen was performed in over 60 consistent speed-tracking experiments. The detailed procedure is shown in Figure 6.

Convert the current data to joint output torque values as follows:

$$T_i = n\eta K_m I_{mi}(i = 1, 2), \quad (21)$$

where n represents the total reduction ratio, with $n = 3060$; η stands for the total transmission efficiency, and $\eta = 82\%$; K_m denotes the sensitivity coefficient, with $K_m = 29.3$ mN·m/A; and I_{mi} refers to the motor current.

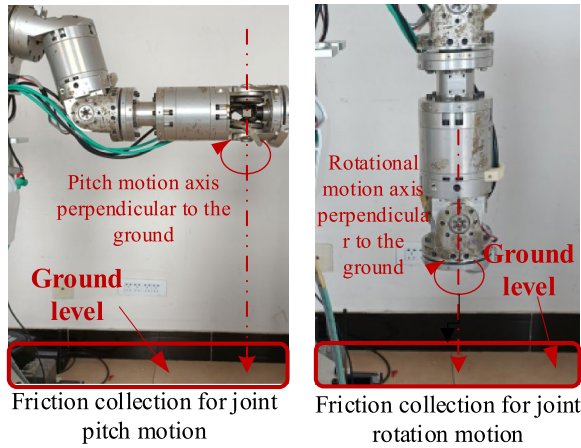Friction collection for joint pitch motion

Friction collection for joint rotation motion

Figure 6 Pose for friction force collection experiment

Table 4 Continuous differentiable friction model parameters for rotation and pitching motion

Parameter	Rotational motion	Pitch motion
γ_1	32.36	39.1
γ_2	9.94	8.65
γ_3	5.25	6.54
γ_4	30.54	10.04
γ_5	10.77	19.71
γ_6	2.68	3.05
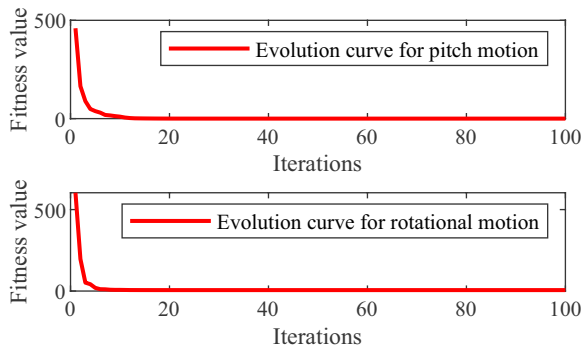
Figure 7 Evolutionary curve of fitness algorithm

(a) Rotational motion friction model

(b) Pitching-motion friction model
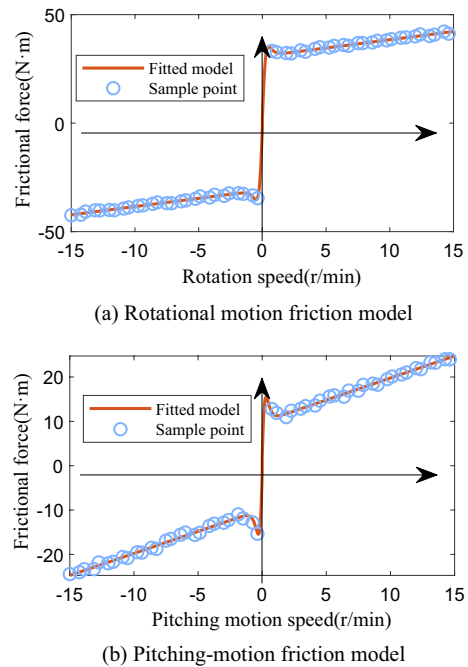
Figure 8 Comparison of the fitted friction model and sampled points

Although traditional identification methods face difficulties in handling nonlinear challenges, this study utilized the Particle Swarm Optimization (PSO) algorithm for this task [33]. Note that the algorithm integrates a compression factor to optimize its global and local search functions, thereby boosting its overall performance. During the identification phase, we designated an iteration limit of 200 and defined a particle dimensionality of six. The objective function depended on the variance between the frictional force captured by the joint and its anticipated counterpart. The primary goal of optimization is to reduce this differential. The fitness curve obtained during the identification process is shown in Figure 7.

The parameters for the continuous differentiable friction model of the yaw and pitching motions are listed in Table 4.

A comparison between the fitted friction model and the actual sampled data is shown in Figure 8.

We employed the goodness-of-fit metric to gauge the precision of identifying the friction model. Specifically,

the R^2 value for the friction model of rotational motion was 0.931, whereas that for the pitch motion was 0.927. These data underscore the excellent performance of the particle swarm optimization algorithm for discerning a continuous friction model.

4.2 Inertia Parameter Identification

Before identifying the inertia parameters, it is essential to establish the excitation trajectory. This trajectory represents the path of the joint motion designed to stimulate the joint dynamic parameters maximally [34]. Within the realm of robot dynamic identification, this excitation trajectory is commonly articulated as a finite-term Fourier series as follows:

Lu *et al. Chinese Journal of Mechanical Engineering*   (2024) 37:74

Page 9 of 15

$$q_i(t) = q_{i0} + \sum_{l=1}^{N} \left(\frac{a_l^i}{\omega_f l} \sin(\omega_f l t) - \frac{b_l^i}{\omega_f l} \cos(\omega_f l t) \right),$$
(22)

where q_i represents the angle of the i-th joint, N represents the Fourier series, and $N=3$ is chosen. ω denotes the fundamental frequency of the trajectory, and in this case, ω_f is set as 0.2π. q_{i0}, a_l^i, b_l^i represents the parameters to be optimized in the excitation trajectory.

During system identification, the selection of the excitation trajectory parameters cannot be arbitrary. This is owing to the constraints that the robot faces, such as joint angles, angular velocities, and angular accelerations, during operation. To ensure the stability and avoid oscillations, the initial angle, angular velocity, and angular acceleration of the excitation trajectory must approach zero. Moreover, the trajectory should be confined to the operational workspace of the robot. Therefore, when setting the parameters for this trajectory, the essential boundary constraints are:

$$\Lambda_{con} = \begin{cases} |q_i(t)| \le q_{i\max}, \\ |\dot{q}_i(t)| \le \dot{q}_{i\max}, \\ |\ddot{q}_i(t)| \le \ddot{q}_{i\max}, \\ q_i(t_0) = q_i(t_f) = 0, \\ \dot{q}_i(t_0) = \dot{q}_i(t_f) = 0, \\ \ddot{q}_i(t_0) = \ddot{q}_i(t_f) = 0, \\ W(q(t)) \subset W_s, \end{cases}$$
(23)

where Λ_{con} denotes the constraint conditions. $q_{i\max}$,$\ddot{q}_{i\max}$, and $\ddot{q}_{i\max}$ signifies the maximum angle, angular velocity, and angular acceleration for the ith joint, respectively. $q_{i\max}, \dot{q}_{i\max}$ and $\ddot{q}_{i\max}$ illustrate the angle, angular velocity, and angular acceleration at the beginning of each cycle of the excitation trajectory, respectively. $q_i(t_f), \dot{q}_i(t_f), \ddot{q}_i(t_f)$ conveys the same parameters but at the conclusion of each cycle. $W(\cdot), W_s$ represents both the workspace function and the overall workspace of the robot.

Within these constraints, we address both linear and nonlinear inequalities. Consequently, determining the coefficients for the optimal excitation trajectory requires a nonlinear algorithm. To optimize the excitation trajectory, this study employed the minimum condition number as the primary criterion. As outlined in this research, the six DOF nursing robot arm had joint motion boundary conditions, as listed in Table 5.

To address the challenge of determining the minimum value for this complex nonlinear function, we used the fmicon function in MATLAB. The relevant parameters derived from the computations are listed in Table 6.

The incentive trajectory obtained from the optimized parameters is shown in Figure 9.

Once the incentive trajectory was determined, the nursing robot was instructed to execute it and collect data on the joint position, velocity, and motor current. Each incentive trajectory lasted 10 s. It was operated over ten continuous cycles to reduce the effects of

Table 5 Motion boundary of the nursing robot

Moving boundary	Joint 1	Joint2	Joint 3	Joint 4	Joint 5	Joint 6
$q_{\min}$/(rad)	$-\pi/2$	$-\pi$	$-\pi/2$	$-\pi$	$-\pi/2$	$-\pi/2$
$q_{\max}$/(rad)	$\pi/2$	π	$\pi/2$	π	$-\pi/2$	$-\pi/2$
$\dot{q}_{\min}$/(rad/s^{-1})	-1.047	-0.524	-0.479	-0.479	-0.479	-0.479
$\dot{q}_{\max}$/(rad/s^{-1})	1.047	0.524	0.479	0.479	0.479	0.479
$\ddot{q}_{\min}$/(rad/s^{-2})	-307.22	-153.61	-187.72	-187.72	-187.72	-187.72
$\ddot{q}_{\max}$/(rad/s^{-2})	307.22	153.61	187.72	187.72	187.72	187.72

Table 6 Excitation trajectory parameters

Para-meter	Joint 1	Joint 2	Joint 3	Joint 4	Joint 5	Joint 6
a_1	0.204	0.163	-0.106	0.058	-0.071	0.031
b_1	0.139	0.208	-0.255	0.038	-0.325	-0.086
a_2	-0.004	-0.106	0.038	-0.007	0.051	-0.021
b_2	-0.440	0.074	-0.055	-0.225	0.017	-0.196
a_3	-0.201	-0.056	0.067	-0.050	0.019	0.019
b_3	0.247	-0.119	0.122	0.137	0.097	0.159
q_0	0.002	0.328	-0.386	-0.045	-0.453	-0.208

(a) Incentive trajectory of end-effector of robot

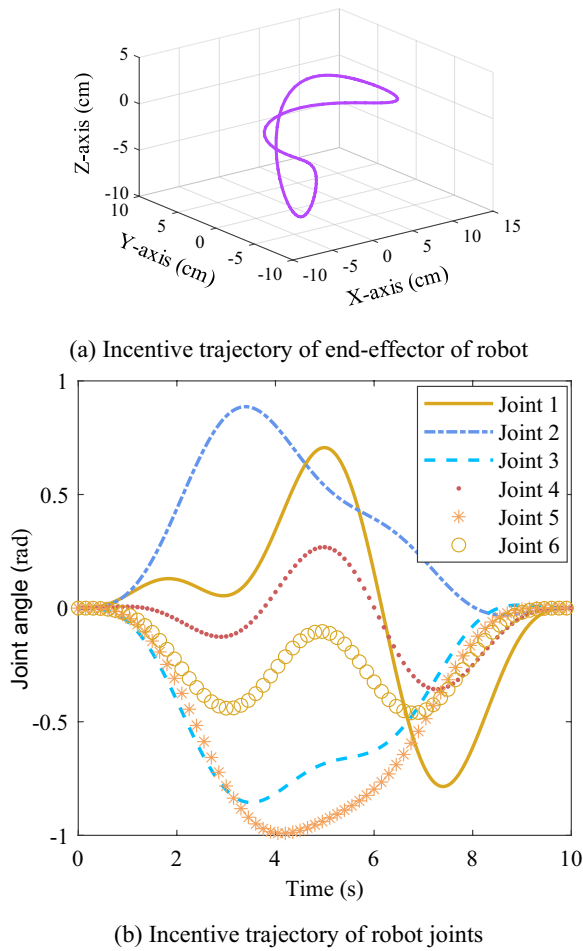(b) Incentive trajectory of robot joints

Figure 9 The incentive trajectory of the nursing robot

measurement noise. The methodology for identifying the inertia parameters of the robotic arm is shown in Figure 10.

The motor-current data exhibited pronounced variation, warranting preliminary filtering. Given its origin in the incentive trajectory, the data should reflect the frequency attributes of the trajectory. To address this, we employed a low-pass Butterworth filter featuring a 0–15 Hz bandwidth and 4 dB ripple for data refinement. The results of this filtering process are shown in Figure 11.

After filtering, the motor current yields the output torque of the motor when multiplied by its sensitivity coefficient. However, in the identification process, the primary focus was on the output torque of the joint. Therefore, conversion of the motor current data to the joint output torque is imperative. This transition necessitates the incorporation of the kinematics, dynamics, and frictional forces specific to the coupled drive joint. A comprehensive depiction of this conversion is shown in Figure 12.

Due to disturbances and various external influences, it is necessary to process the directly collected data for noise reduction. Considering the cyclical nature of the incentive trajectory, we implement mean filtering of the signal within each cycle as follows:

$$
\begin{cases}
\overline{q}_1(k) = \frac{1}{N_j}\sum\limits_{i=1}^{N_j} q_{1i}(k), & \overline{q}_2(k) = \frac{1}{N_j}\sum\limits_{i=1}^{N_j} q_{2i}(k), \\
\overline{\dot{q}}_1(k) = \frac{1}{N_j}\sum\limits_{i=1}^{N_j} \dot{q}_{1i}(k), & \overline{\dot{q}}_2(k) = \frac{1}{N_j}\sum\limits_{i=1}^{N_j} \dot{q}_{2i}(k), \\
\overline{\tau}_{f1}(k) = \frac{1}{N_j}\sum\limits_{i=1}^{N_j} \tau_{f1i}(k), & \overline{\tau}_{f2}(k) = \frac{1}{N_j}\sum\limits_{i=1}^{N_j} \tau_{f2i}(k), \\
\overline{T}_{mc1}(k) = \frac{1}{N_j}\sum\limits_{i=1}^{N_j} T_{mc1i}(k), & \overline{T}_{mc2}(k) = \frac{1}{N_j}\sum\limits_{i=1}^{N_j} T_{mc2i}(k),
\end{cases}
\tag{24}
$$

where K represents the number of sampling times within each cycle, N_j is the number of cycles in the incentive trajectory, $q_{1i}(k)$, $q_{2i}(k)$ represents the yaw and pitch joint angles, $\tau_{f1i}(k)$, $\tau_{f2i}(k)$ signifies the yaw and pitch frictional forces, and $T_{mc1}(k)$, $T_{mc2}(k)$ corresponds to the yaw and pitch joint output torques. Therefore, the robot's output torque can be expressed as follows:

$$
\begin{cases}
\boldsymbol{\tau} = [\tau_1, \tau_2, \tau_3, \tau_4, \tau_5, \tau_6]^{\mathrm{T}}, \\
\tau_i = \overline{T}_{mc1} - \overline{\tau}_{fi}, \ i = 1 \sim 6.
\end{cases}
\tag{25}
$$

Utilizing Eq. (16), we form a dataset where the joint torque observation matrix $\boldsymbol{\tau}$ serves as the target and the coefficient matrix $\tilde{Y}(\boldsymbol{q}, \dot{\boldsymbol{q}}, \ddot{\boldsymbol{q}})$ acts as the features. Of this dataset, 70% was designated for training, and the remaining 30% for testing. Once standardized, the curated dataset was input into a ridge regression model for training. The dynamic inertial parameters of the identified robotic arm are listed in Table 7.

5 Experiment

In transfer care, caregivers are primarily responsible for moving patients from their beds to wheelchairs and addressing essential needs such as restroom use, feeding, and mobility. To simulate this, we created the experimental scenario shown in Figure 13. To address these multifaceted challenges, our dual-arm care robot was engineered to control several motors in unison, necessitating exceptional real-time responsiveness, functionality, and stability from its controller. To achieve this, we integrated the robot's control system with the EtherCAT fieldbus by selecting the Elmo MOLTWI-10/100EEOT driver and an Apache industrial PC with an i7-8700 processor as the central control unit. Moreover, this control unit offers remote operability, enabling distant management of care robots.
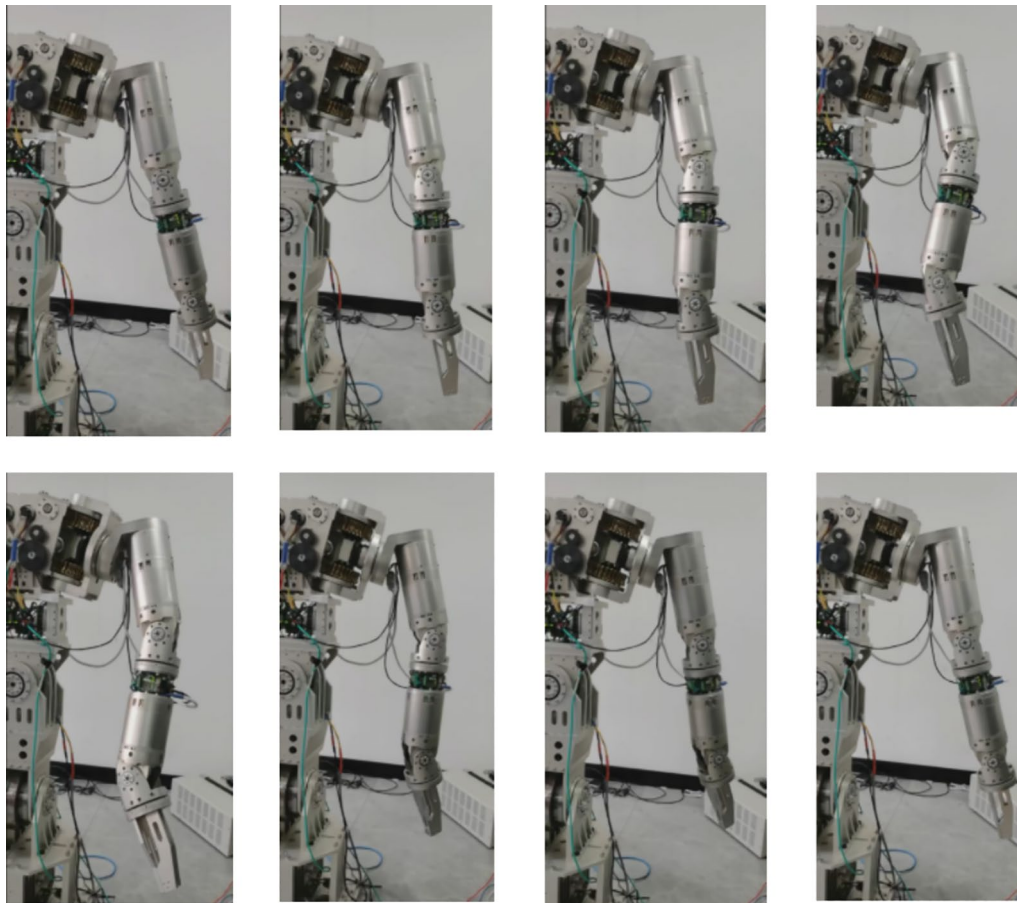
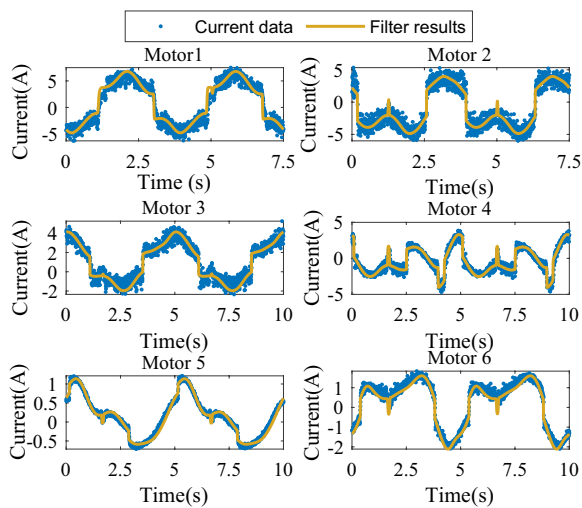**Figure 10** Inertial parameter identification process
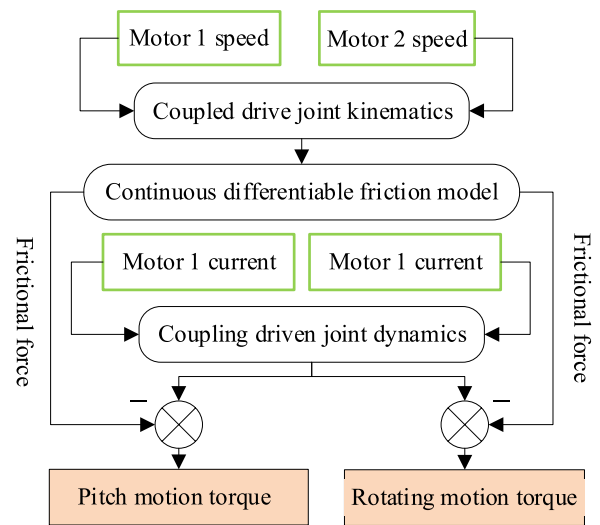

Figure 11 Current data filtering

Figure 12 The conversion process of output torque

Table 7 Identified inertia parameters

Inertial parameters	Identification value	Inertial parameters	Identification value
I_{zz1}	49.53	I_{yz4}	−1.215
I_{xx2r}	10.417	I_{zz4r}	81.610
I_{xy2r}	23.183	mx_4	79.431
I_{xz2}	−28.211	my_{4r}	1.927
I_{yz2}	−0.219	I_{xx5r}	1.724
I_{zz2r}	−0.225	I_{xy5}	1.455
mx_{2r}	8.327	I_{xz5}	0.816
my_{2r}	30.219	I_{yz5}	0.957
I_{xx3r}	50.231	I_{zz5r}	2.121
I_{xy3}	9.006	mx_5	−2.103
I_{xz3}	7.183	my_{5r}	15.450
I_{yz3}	46.124	I_{xx6r}	1.060
I_{zz3r}	−1.212	I_{xy6}	−2.013
mx_3	1.215	I_{xz6}	20.791
my_{3r}	−1.231	I_{yz6}	−1.142
I_{xx4r}	4.134	I_{zz6}	1.095
I_{xy4}	16.289	mx_6	1.921
I_{xz4}	19.316	my_6	−1.528

Figure 14 Verify trajectory

Figure 13 Experimental scenario

Figure 15 Verification of Dynamic Parameter Identification
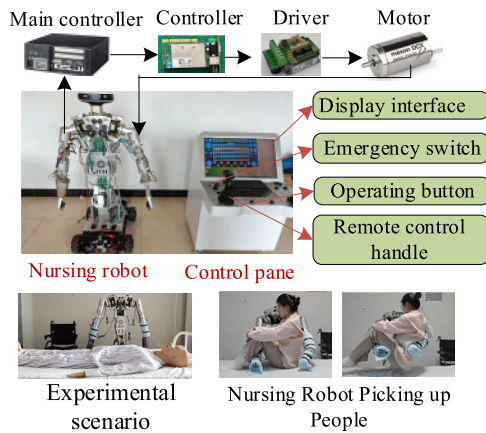
To validate the accuracy of the identification results, the robotic arm was directed to follow a verification trajectory that differed from the original stimulation trajectory. We then assessed the alignment between the computed joint torques and the actual measured values. The verification trajectory presented in this study was formulated by adjusting the coefficients of the stimulation trajectory, as shown in Figure 14.

We captured motor current and speed data from the robotic arm. Drawing on the coupled drive joint dynamics model, friction model, and the discerned parameters for both the joint dynamics and friction models, we
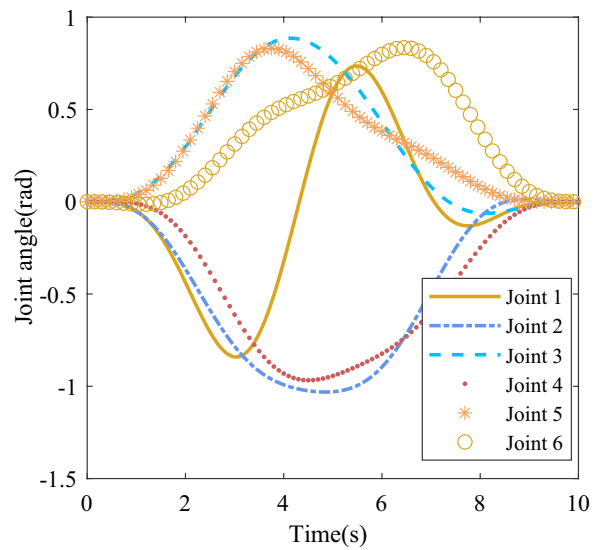
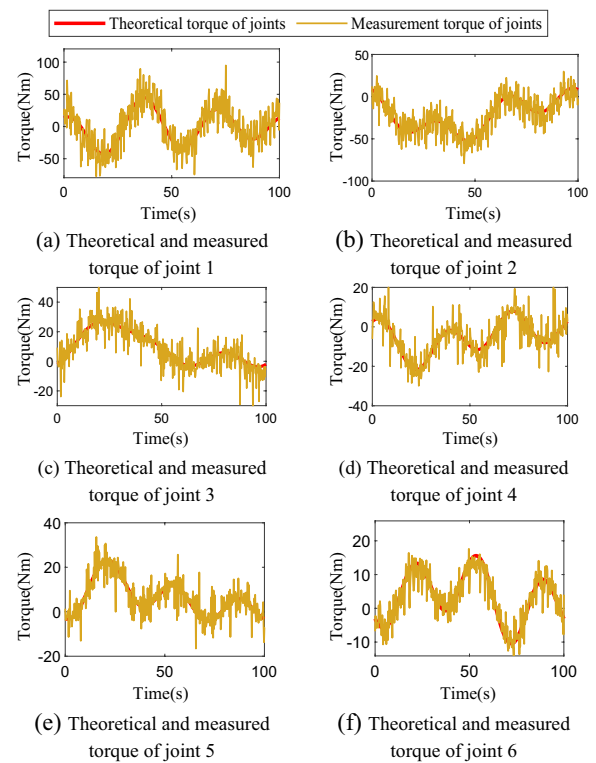determined the joint torque and treated it as the measured value. Throughout this procedure, we employed the noise-reduction filtering algorithm outlined in Section 4.2 to refine the motor current and speed data. Next, by leveraging the recognized inertia parameters of the

robotic arm and its linearized dynamic model, we computed the theoretical joint torque. Finally, we juxtaposed the measured torque with its theoretical counterpart, as shown in Figure 15.

To evaluate the accuracy of the identification results, the root mean square errors (RMSE) of the actual and theoretical torques were used as a quantitative metric. The torque root mean square error can be expressed as follows:

$$\varepsilon_{RMS,i} = \sqrt{\frac{1}{k_n} \sum_{k=1}^{k_n} (\hat{H}_i(k) - H_i(k))^2}, i = 1 \sim 6, \quad (26)$$

where $\varepsilon_{RMS,i}$ represents the root mean square error of each joint, k_n denotes the number of sampling points, $\hat{H}_i(k)$ represents the predicted joint torque, $H_i(k)$ represents the measured joint torque, and i represents the joint index. The RMSE between the measured and theoretical torques for each joint are listed in Table 8.

As listed in Table 8, it is evident that the root mean square error between the measured and theoretical torques is notably small when juxtaposed with the joint drive torque. This underscores the precision of the dynamic parameter identification shown in Figure 15, thereby attesting to the efficacy of the proposed dynamic modeling and identification techniques. Furthermore, fluctuations in the measured torque surrounding the theoretical values are shown in Figure 15, indicating discrepancies between the dynamic identification outcomes and the anticipated results. These discrepancies likely arose from pronounced variations in the motor current and the intricate design of the robotic arm. The dynamic model, which is based on a streamlined mechanical representation, neglects elements such as lubrication and the impact of gear meshing. In addition, imperfections during the machining and assembly phases introduce gaps between the transmission components, further influencing the precision of identification.

Table 8 The RMSE between the measured and theoretical torques for each joint

Joint ID	RMSE (N·m²)
Joint 1	14.372
Joint 2	11.982
Joint 3	6.934
Joint 4	5.557
Joint 5	3.932
Joint 6	3.152

6 Discussion

Dynamic modeling and parameter identification are essential for achieving dynamic, compliant interactions between robots and humans. This study focuses on an innovative coupled-drive joint and explores its dynamic modeling, robotic arm dynamic modeling, friction model, friction model parameter identification, and inertia parameter identification methods. The accuracy of these methods was validated through experiments.

However, there are noticeable discrepancies between the experimentally collected and theoretical data. These discrepancies stem from unavoidable simplifications made during the mathematical modeling process, such as assuming uniform materials for components, ignoring machining errors, and neglecting the influence of small-inertia parts. Although identifying model parameters through actual data partially compensates for these modeling errors, it does not fundamentally resolve the mismatch between the actual working conditions and theoretical derivations.

Given that humans possess a certain degree of environmental adaptability, ensuring that the gap between actual conditions and theoretical derivations remains within a specific range allows robots to be effectively applied in human-robot interaction tasks. Therefore, despite errors, the methods presented in this study remain feasible. In the future, we plan to transcend the current research framework and construct dynamic models of complex human-robot systems entirely using data-driven methods.

7 Conclusions

This study explored methods for the dynamic modeling and parameter identification of a coupled drive joint robotic arm. The accuracy of these methods was validated through trajectory-tracking experiments using a nursing robot. The key findings are as follows:

(1) The dynamic model of the coupled-drive nursing robot comprises two parts: the joint dynamics model and the robotic arm dynamics model. The joint dynamics model describes the relationship between the motor torque and joint torque, whereas the robotic arm dynamics model describes the relationship between the joint torque and robot motion.

(2) By designing experiments to compensate for the effects of gravity, inertia, and modeling errors, friction can be represented using directly collected current data. The particle swarm optimization algorithm demonstrated high accuracy in identifying the friction model parameters. In this study, the coefficient of determination (R^2) for joint turnover friction was 0.931, and for joint pitch friction was 0.927.

Lu *et al. Chinese Journal of Mechanical Engineering*　　(2024) 37:74

Page 14 of 15

(3) The Fourier excitation trajectory, optimized according to the robot's motion constraints, effectively identifies the inertial parameters of the dynamic model. In this study, the root mean square error (RMSE) for the inertial parameter identification of joint 1 (base joint) is 14.372 N·m^2, and for joint 6 (end joint) is 3.152 N·m^2.

Declarations

Competing Interests
The authors declare no competing financial interests.

References
[1] http://www.stats.gov.cn/sj/zxfb/202302/t20230203_1901080.html.
[2] N Chivarov, D Chikurtev, S Chivarov, et al. Case study on human-robot interaction of the remote-controlled service robot for elderly and disabled care. *Computing and Informatics*, 2019, 38(5): 1210-1236.
[3] D Portugal, P Alvito, E Christodoulou, et al. A study on the deployment of a service robot in an elderly care center. *International Journal of Social Robotics*, 2019, 11: 317-341.
[4] R Wu, J Wang, W Chen, et al. Design of a transfer robot for the assistance of elderly and disabled. *Advanced Robotics*, 2021, 35(3-4): 194-204.
[5] J Yang, Z Song, R Wu, et al. Design of lifting mechanism of transfer robot for the elderly. 2022 *IEEE International Conference on Real-time Computing and Robotics (RCAR)*. IEEE, 2022: 568-572.
[6] M A Salichs, Á Castro-González, E Salichs, et al. Mini: a new social robot for the elderly. *International Journal of Social Robotics*, 2020, 12: 1231-1249.
[7] W Tian, H Yin, D Chen, et al. The Mechatronic system design of the bed-chair integration system E-Bed. *2021 IEEE 16th Conference on Industrial Electronics and Applications (ICIEA)*. IEEE, 2021: 1990–1995.
[8] K K Santhanaraj, R MM. A survey of assistive robots and systems for elderly care. *Journal of Enabling Technologies*, 2021, 15(1): 66-72.
[9] N Lv, J Liu, Y Jia. Dynamic modeling and control of deformable linear objects for single-arm and dual-arm robot manipulations. *IEEE Transactions on Robotics*, 2022, 38(4): 2341-2353.
[10] Q Guan, Z Yang, H Lu, et al. Analysis of comfort during transfer by a dual-arm care robot based on human body pressure and surface electromyographic signals. *Bioengineering*, 2023, 10(8): 903.
[11] M Q Chen, J Wu, S Li, et al. Accurate and real-time human-joint-position estimation for a patient-transfer robot using a two-level convolutional neutral network. *Robotics and Autonomous Systems*, 2021, 139: 103735.
[12] Y Li, S Guo, Z Gan. Empirical prior based probabilistic inference neural network for policy learning. *Information Sciences*, 2022, 615: 678-699.
[13] S S Han, H P Wang, H Y Yu. Human–robot interaction evaluation-based AAN control for upper limb rehabilitation robots driven by series elastic actuators. *IEEE Transactions on Robotics*, 2023, 39(5): 3437-3451
[14] Y Li, S Y Feng, D L Zhu, et al. Behavioral safety control of redundant dual arm robots for transfer nursing. *Journal of Mechanical Engineering*, 2023, 59 (9): 76-89. (in Chinese)
[15] K Wang, H Qian, Y Yang, et al. A novel differential modular robot joint—design and implementation. *2013 IEEE International Conference on Robotics and Biomimetics (ROBIO)*. IEEE, 2013: 2049-2054.
[16] H Lu, S J Guo, Z Q Yang, et al. Dynamic modeling and parameter identification of 2r coupled drive joint. *Journal of Mechanical Engineering*, 2022, 58 (23): 51-64. (in Chinese)
[17] M C Olarui, S Krut, F Pierrot. Novel mechanical design of biped robot SHERPA using 2 DOF cable differential modular joints. *IEEE/RSJ International Conference on Intelligent Robots & Systems*, IEEE, 2009: 4463–4468.
[18] U Hagn, M Nickl, S Jrg, et al. The DLR MIRO: A versatile lightweight robot for surgical applications. *Industrial Robot*, 2008, 35(08): 324-336.
[19] Z H Xu, S Li, X F Zhou, et al. Dynamic neural networks for motion-force control of redundant manipulators: An optimization perspective. *IEEE Transactions on Industrial Electronics*, 2020, 68(2): 1525-1536.
[20] K Chatzilygeroudis, V Vassiliades, F Stulp, et al. A survey on policy search algorithms for learning robot controllers in a handful of trials. *IEEE Transactions on Robotics*, 2019, 36(2): 328-347.
[21] W Xu, T Liu, Y Li. Kinematics, dynamics, and control of a cable-driven hyper-redundant manipulator. *IEEE/ASME Transactions on Mechatronics*, 2018, 23(4): 1693-1704.
[22] W Xiang, S Yan. Dynamic analysis of space robot manipulator considering clearance joint and parameter uncertainty: Modeling, analysis and quantification. *Acta Astronautica*, 2020, 169: 158-169.
[23] X Che, H Yu, C Zhang, et al. The effect of floating spline parameter on the dynamic characteristic of encased differential planetary gear train. *Scientific Reports*, 2024, 14(1): 8349.
[24] E Corral, M J G García, C Castejon, et al. Dynamic modeling of the dissipative contact and friction forces of a passive biped-walking robot. *Applied Sciences*, 2020, 10(7): 2342.
[25] L Hao, R Pagani, M Beschi, et al. Dynamic and friction parameters of an industrial robot: Identification, comparison and repetitiveness analysis. *Robotics*, 2021, 10(1): 49.
[26] C Ren, X Li, X Yang, et al. Extended state observer-based sliding mode control of an omnidirectional mobile robot with friction compensation. *IEEE Transactions on Industrial Electronics*, 2019, 66(12): 9480-9489.
[27] J Dong, J Xu, Q Zhou, et al. Dynamic identification of industrial robot based on nonlinear friction model and LS-SOS algorithm. *IEEE Transactions on Instrumentation and Measurement*, 2021, 70: 1-12.
[28] J Xiao, S Dou, W Zhao, et al. Sensorless human-robot collaborative assembly considering load and friction compensation. *IEEE Robotics and Automation Letters*, 2021, 6(3): 5945-5952.
[29] M Safeea, P Neto, R Bearee. Robot dynamics: A recursive algorithm for efficient calculation of Christoffel symbols. *Mechanism and Machine Theory*, 2019, 142: 103589.
[30] C Makkar, W E Dixon, W G Sawyer, et al. A new continuously differentiable friction model for control systems design. *IEEE/ASME International Conference on Advanced Intelligent Mechatronics*. IEEE, 2005: 600–605.
[31] N T Hegde, V I George, C G Nayak, et al. Design, dynamic modelling and control of tilt-rotor UAVs: A review. *International Journal of Intelligent Unmanned Systems*, 2020, 8(3): 143-161.
[32] C Gaz, M Cognetti, A Oliva, et al. Dynamic identification of the franka emika panda robot with retrieval of feasible parameters using penalty-based optimization. *IEEE Robotics and Automation Letters*, 2019, 4(4): 4147-4154.
[33] L Zhang, Y Zhang, Y Li. Mobile robot path planning based on improved localized particle swarm optimization. *IEEE Sensors Journal*, 2020, 21(5): 6962-6972.
[34] T Lee, B D Lee, F C Park. Optimal excitation trajectories for mechanical systems identification. *Automatica*, 2021, 131: 109773.

Hao Lu　born in 1990, is currently a lecturer at the *College of Electronic Information and Automation, Tianjin University of Science and*

Lu *et al. Chinese Journal of Mechanical Engineering*　　(2024) 37:74

Page 15 of 15

Technology, China. His research interests include intelligent nursing-care and rehabilitation robotics.

Zhiqiang Yang　born in 1992, is currently a PhD candidate at *Academy for Engineering & Technology, Fudan University, China*. His research interests include nursing-care intelligent robotics.

Deliang Zhu　born in 1998, is currently a PhD candidate at *Academy for Engineering & Technology, Fudan University, China*. His research interests include nursing-care intelligent robotics.

Fei Deng　born in 1997, is currently a master candidate at *College of Mechanical Engineering, Hebei University of Technology, China*. His research interests include nursing-care intelligent robotics.

Shijie Guo　born in 1963, is currently a professor and a PhD candidate supervisor at *Academy for Engineering & Technology, Fudan University, China*. His main research interests include nursing-care intelligent robotics, unbound physiological health information monitoring, tactile perception of robot.